Frequency-domain sensitivity analysis for small imaging domains using the equation of radiative transfer

Xuejun Gu, Kui Ren, and Andreas H. Hielscher

Optical tomography of small imaging domains holds great promise as the signal-to-noise ratio is usually high, and the achievable spatial resolution is much better than in large imaging domains. Emerging applications range from the imaging of joint diseases in human fingers to monitoring tumor growth or brain activity in small animals. In these cases, the diameter of the tissue under investigation is typically smaller than 3 cm, and the optical path length is only a few scattering mean-free paths. It is well known that under these conditions the widely applied diffusion approximation to the equation of radiative transfer (ERT) is of limited applicability. To accurately model light propagation in these small domains, the ERT has to be solved directly. We use the frequency-domain ERT to perform a sensitivity study for small imaging domains. We found optimal source-modulation frequencies for which variations in optical properties, size, and location of a tissue inhomogeneity lead to maximal changes in the amplitude and phase of the measured signal. These results will be useful in the design of experiments and optical tomographic imaging systems that probe small tissue volumes.

OCIS codes: 170.0170, 170.3880, 170.6960.

1. Introduction

Big strides have been made over the past ten years toward optical tomographic imaging of biological tissues.[1–3] With the emergence of the appropriate light detection technology and suitable image reconstruction codes, the field has increasingly focused on clinical and preclinical applications. Besides human breast and brain imaging, which involve light transmission across large tissue volumes (~25 to 1000 cm^3), the imaging of small tissue volumes (~1 to 25 cm^3) is of great interest in many areas. Applications range from imaging joint diseases in human fingers[4,5] to monitoring tumor growth and brain activity in small animals.[6] Because of the small geometries involved, a considerable amount of light transmits those tissues. And unlike in optical breast or brain imaging, the signal-to-noise ratio level is relatively high.

While the signal levels are typically high, imaging small tissue volumes is far from trivial. The main challenge here is that the diffusion approximation, which is typically used to model light propagation in larger tissue structures, becomes less accurate. The number of scattering events between sources and detectors decreases as the medium of interest becomes smaller; consequently, the equation of radiative transfer (ERT), and not its diffusion approximation, needs to be solved to accurately model light propagation.

Only a limited number of groups have attempted to solve the ERT for problems encountered in optical tomography because implementing an efficient and accurate ERT algorithm is considerably more challenging than using the diffusion equation. Works include solutions to the 2D time-dependent and time-independent ERT[7,8] and the 3D time-independent ERT.[9–12] Recently, our group introduced what we believe to be the first frequency-domain ERT code that can be used for optical tomographic imaging.[13,14] In general it is believed that frequency-domain algorithms can provide better separations of absorption and scattering effects compared to steady-state or cw methods. This belief has been supported by both theoretical[15] and numerical[14,16] evidence in recent years.

In the study at hand we use the frequency-domain ERT code to investigate the detection limits of tissue inhomogeneities with varying optical properties, sizes, and locations. Similar studies have been performed before but did not focus on small tissue volumes and did not use the ERT as a light-propagation

The authors are with Columbia University, New York, New York 10027. X. Gu and A. H. Hielscher (ahh2004@columbia.edu) are with the Department of Biomedical Engineering. A. H. Hielscher is also with the Department of Radiology. K. Ren is with the Department of Applied Physics and Applied Mathematics.

Received 27 June 2006; accepted 7 August 2006; posted 22 September 2006 (Doc. ID 72290); published 13 March 2007.

0003-6935/07/101624-09$15.00/0

model. For example, Boas *et al.*[17] studied the effect of the source-modulation frequency on the quantification and localization accuracy of scattering and absorbing perturbation in a 60 mm thick infinite slab, which mimicked light propagation in female breast tissue. Their analysis was based on analytical solution for the frequency-domain diffusion equation. Toronov *et al.*[18] analyzed the signal-sensitivity-to-noise ratio (SSNR) of phase measurement at different modulation frequencies using Monte Carlo simulation of light propagation in the human head. Sensitivity studies for fluorescence tomography were presented by Eppstein *et al.*[19] By performing sensitivity studies particular for small tissue geometries using the frequency ERT, our work provides an important insight into the potentials and limitations of small tissue tomography and will help in the design of appropriate experimental setups and tomographic instrumentation.

In Section 2 we provide some theoretical and experimental background for our analysis and define the terms signal-to-noise ratio (SNR) and SSNR. In Section 3 we present our numerical analysis, which is followed in Section 4 by a discussion of the results.

2. Signal and Noise Model

First we formulate the numerical model of the light transport with the ERT and set up the discretization formulation. The theoretical foundation for the sensitivity analysis based on this forward model is presented, and the shot-noise-dominant noise model is given. Finally the SNR and the SSNR of the forms are defined.

A. Theoretical Background of Signal and Signal Sensitivity Based on the Equation of Radiative Transfer

The frequency-domain ERT that describes the photon density in the phase space, i.e., as a function of position $\mathrm{x} \in \mathcal{D} \subset \mathbb{R}^3$ and direction $\boldsymbol{\theta} \in S^2$ (unit sphere of $\mathbb{R}^3$), is given by[13]

$$\left[-\frac{i\omega}{v} + \boldsymbol{\theta}\nabla + \mu_t(\mathbf{x})\right]\psi(\mathbf{x},\ \boldsymbol{\theta}) - \mu_s(\mathbf{x}) \times \int_{S^2} k(\boldsymbol{\theta}\boldsymbol{\theta}')\psi(\mathrm{x},\ \boldsymbol{\theta}')\mathrm{d}\boldsymbol{\theta}' = 0 \qquad \text{in } \mathcal{D} \times S^2$$

$$\psi(\mathbf{x},\ \boldsymbol{\theta}) = q(\mathbf{x},\ \boldsymbol{\theta}) \quad \text{on } \Gamma_-. \tag{1}$$

Here $i = \sqrt{-1}$, v is the speed of light in the medium, and ω is the source-modulation frequency. The parameter $\mu_t = \mu_a + \mu_s$, with μ_a and μ_s being the absorption and scattering coefficients, respectively. $\psi(\mathbf{x}, \boldsymbol{\theta})$ is the radiance at position $\mathbf{x}$ traveling in direction $\boldsymbol{\theta}$ with the unit of $\mathrm{W\,m^{-2}sr^{-1}}$; here note that $\psi(\mathbf{x}, \boldsymbol{\theta})$ is frequency dependent. $q(x, \theta)$ is the source with the unit of $\mathrm{W\,m^{-3}sr^{-1}}$ defined on the boundary set

$$\Gamma_{\pm} = \{(\mathbf{x},\ \boldsymbol{\theta}) \in \partial\mathcal{D} \times S^2 \text{ such that } \pm\,\boldsymbol{\theta}\boldsymbol{\nu}(\mathbf{x}) > 0\},$$

with $\boldsymbol{\nu}(\mathbf{x})$ the outward unit normal to the domain at $\mathbf{x} \in \partial\mathcal{D}$. The scattering kernel $k(\boldsymbol{\theta}\boldsymbol{\theta}')$, which describes the probability that photons traveling in direction $\boldsymbol{\theta}'$ scatter into direction $\boldsymbol{\theta}$, is a positive function independent of $\mathbf{x}$. The scattering kernel for light propagation in tissues is chosen here as the Henyey–Greenstein phase function[20,21]

$$k(\boldsymbol{\theta}\boldsymbol{\theta}') = \frac{1 - g^2}{(1 + g^2 - 2g\cos\phi)^{3/2}}, \tag{2}$$

where ϕ is the angle between $\boldsymbol{\theta}$ and $\boldsymbol{\theta}'$, i.e., $\boldsymbol{\theta}\boldsymbol{\theta}' = \cos\phi$ and $g \in [-1, 1]$ is the so-called anisotropy factor. The larger g is, the more forward directed is the scattering; for $g = 0$ the scattering is isotropic. The reduced or transport scattering coefficient is given by $\mu_s' = (1 - g)\mu_s$. The scattering kernel satisfies the normalization condition $\int_{S^2} k(\boldsymbol{\theta}\boldsymbol{\theta}')\mathrm{d}\boldsymbol{\theta}' = 1$.

Solving Eq. (1) results in a value for the radiance ψ. In the optical tomography experiments, however, one typically measures the outgoing current, which is given by

$$J(\mathbf{x}_d) = \int_{S_+^2} \boldsymbol{\theta}\nu(\mathbf{x}_d)\psi(\mathbf{x}_d,\ \boldsymbol{\theta})\mathrm{d}\boldsymbol{\theta}. \tag{3}$$

Here $\mathbf{x}_d$ is the position of detector $S_+^2 = \{\boldsymbol{\theta} : \boldsymbol{\theta} \in S^2$, and $\boldsymbol{\theta}\nu(\mathbf{x}_d) > 0\}$. The outgoing current $J(\mathbf{x}_d)$ is a complex functional of optical parameters μ_a and μ_s.

If we denote $(\delta\mu_a, \delta\mu_s)$ as the perturbation of (μ_a, μ_s), we can define the signal sensitivity as

$$\delta J(\mathbf{x}_d)(\delta\mu_a,\ \delta\mu_s) = \int_{S_+^2} \boldsymbol{\theta}\boldsymbol{\nu}(\mathbf{x}_d)\delta\psi(\mathbf{x}_d,\ \boldsymbol{\theta})\mathrm{d}\boldsymbol{\theta}. \tag{4}$$

After a perturbation over the transport solution, we obtain the following transport equation for $\delta\psi$:

$$\left(-\frac{i\omega}{v} + \boldsymbol{\theta}\nabla + \mu_t(\mathbf{x})\right)\delta\psi(\mathbf{x},\ \boldsymbol{\theta}) = \mu_s(\mathbf{x})\int_{S^2} k(\boldsymbol{\theta}\boldsymbol{\theta}')\delta\psi(\mathbf{x},\ \boldsymbol{\theta}')\mathrm{d}\boldsymbol{\theta}' - (\delta\mu_a(\mathbf{x}) + \delta\mu_s(\mathbf{x}))\psi(\mathrm{x},\ \boldsymbol{\theta}) + \delta\mu_s(\mathbf{x})\int_{S^2} k(\boldsymbol{\theta}\boldsymbol{\theta}')\psi(\mathbf{x},\ \boldsymbol{\theta}') \times \mathrm{d}\boldsymbol{\theta}', \tag{5}$$

with the boundary condition

$$\delta\psi(\mathbf{x},\ \boldsymbol{\theta}) = 0 \quad \text{on } \Gamma_-. \tag{6}$$

We now introduce the adjoint transport Green's function $G(\mathbf{x}, \boldsymbol{\theta}; \mathbf{x}_d, \boldsymbol{\theta}_d)$, which solves the following transport equation:

$$\left(-\frac{i\omega}{v}-\boldsymbol{\theta}\nabla+\mu_t(\mathbf{x})\right)G(\mathbf{x},\ \boldsymbol{\theta};\ \mathbf{x}_d,\ \boldsymbol{\theta}_d)=\mu_s(\mathbf{x})\int_{S^2}k(\boldsymbol{\theta}\boldsymbol{\theta}')\times G(\mathbf{x},\ \boldsymbol{\theta};\ \mathbf{x}_d,\ \boldsymbol{\theta}_d)\times \mathrm{d}\boldsymbol{\theta}', \quad (7)$$

with the boundary condition

$$G(\mathbf{x},\ \boldsymbol{\theta};\ \mathbf{x}_d,\ \boldsymbol{\theta}_d)=\delta(\boldsymbol{\theta}-\boldsymbol{\theta}_d)\delta(\mathbf{x}-\mathbf{x}_d)\quad \text{on } \Gamma_+. \quad (8)$$

If we multiply Eq. (5) by $G(\mathbf{x}, \boldsymbol{\theta}; \mathbf{x}_d, \boldsymbol{\theta}_d)$, multiply Eq. (7) by $\delta\psi$, and use integration by parts over the two equations, we obtain

$$\delta\psi(\mathbf{x}_d,\ \boldsymbol{\theta}_d)=\int_X G(\mathbf{x},\ \boldsymbol{\theta};\ \mathbf{x}_d,\ \boldsymbol{\theta}_d)\Bigg[-(\delta\mu_a(\mathrm{x})+\delta\mu_s(\mathrm{x}))\psi(\mathbf{x},\ \boldsymbol{\theta})+\delta\mu_s(\mathbf{x})\times\int_{S^2}k(\boldsymbol{\theta}\boldsymbol{\theta}')\psi(\mathbf{x},\ \boldsymbol{\theta}')\mathrm{d}\boldsymbol{\theta}'\Bigg]\mathrm{d}\mathbf{x}\mathrm{d}\boldsymbol{\theta}, \quad (9)$$

where short notation $X = \mathcal{D} \times S^2$ has been used. This tells us that the signal sensitivity is given by

$$\delta J(\mathbf{x}_d)(\delta\mu_a,\ \delta\mu_s)=\int_{\mathcal{D}}(\Phi_a(\mathbf{x};\ \mathbf{x}_d)\delta\mu_a(\mathbf{x})+\Phi_s(\mathbf{x};\ \mathbf{x}_d)\delta\mu_s(\mathbf{x}))\mathrm{d}\mathbf{x}, \quad (10)$$

with

$$\Phi_a(\mathbf{x};\ \mathbf{x}_d)=-\int_{S_+^2}\boldsymbol{\theta}_d\boldsymbol{\nu}\int_{S^2}G(\mathbf{x},\ \boldsymbol{\theta};\ \mathbf{x}_d,\ \boldsymbol{\theta}_d)\psi(\mathrm{x},\ \boldsymbol{\theta})\mathrm{d}\boldsymbol{\theta}\mathrm{d}\boldsymbol{\theta}_d, \quad (11)$$

$$\Phi_s(\mathbf{x};\ \mathbf{x}_d)=-\int_{S_+^2}\boldsymbol{\theta}_d\boldsymbol{\nu}\int_{S^2}G(\mathbf{x},\ \boldsymbol{\theta};\ \mathbf{x}_d,\ \boldsymbol{\theta}_d)\times\left(\psi(\mathbf{x},\ \boldsymbol{\theta})-\int_{S^2}k(\boldsymbol{\theta}\boldsymbol{\theta}')\psi(\mathbf{x},\ \boldsymbol{\theta}')\mathrm{d}\boldsymbol{\theta}'\right)\times\mathrm{d}\boldsymbol{\theta}\mathrm{d}\boldsymbol{\theta}_d. \quad (12)$$

The functions $\Phi_a(\mathbf{x}; \mathbf{x}_d)$ and $\Phi_s(\mathbf{x}; \mathbf{x}_d)$ are the absorption and scattering sensitivity functions, respectively.[7] Here we are interested in the dependences of those functions on the source-modulation frequency and the location, diameter, and contrast of an optical inhomogeneity. A look at the above asymptotics tells us that the signal sensitivity (δJ) in the measured data includes contributions from the perturbation of absorption and of scattering. As can be seen from Eq. (10), the signal sensitivity (δJ) can be separated into the perturbation with absorption coefficient ($\delta\mu_a$) and the scattering coefficient ($\delta\mu_s$). This separation will allow us later to discuss the absorption and scattering effects independently.

Although the theoretical analysis above yields the analytical formula of the signal and the signal sensitivity, seldom is the analytical solution of the ERT available. With the combination of the discrete ordinates method[22] for the angular variable and a finite-volume discretization method for the space variable,[23] the ERT can be converted to the following algebraic equation:

$$\mathbf{A}\boldsymbol{\Psi}=\mathbf{S}\boldsymbol{\Psi}+\mathbf{Q}, \quad (13)$$

where $\mathbf{A}$ and $\mathbf{S}$ are discretized streaming-collision and scattering operators, and $\mathbf{Q}$ is a discretized source term. This algebraic Eq. (13) can be solved by a restarted generalized minimal residual (GMRES) algorithm.[24] More details concerning the implementation of the discrete ordinates method for this specific problem can be found in Ref. 13.

B. Experimental Background of Signal, Signal Sensitivity, and Noise

With fiber-based optical experimental measurement, the flux $J(\mathbf{x}_d)$ (signal measured) is the summation of the radiance's components on the boundary normal direction. In the frequency-domain measurement, the signal, consisting of amplitude (AC) and phase delay (ϕ), can be explicitly written as

$$J(\mathbf{x}_d)(\mu_a,\ \mu_s)=\mathrm{AC}\ \exp(i\phi). \quad (14)$$

Here AC and ϕ refer to measured amplitude and phase. Consequently, the signal sensitivity $\delta J(\mathbf{x}_d)$ defined as the signal caused by the optical properties' perturbation is

$$\delta J(\mathbf{x}_d)(\delta\mu_a,\ \delta\mu_s)=\mathrm{AC}^t\exp(i\phi^t)-\mathrm{AC}^h\exp(i\phi^h), \quad (15)$$

where AC^t, ϕ^t are the amplitude and phase with perturbation and AC^h, ϕ^h are the amplitude and phase without perturbation. Considering that the physically measured signals are denoted as amplitude and phase we define the signal amplitude sensitivity (δAC) and signal phase sensitivity ($\delta\phi$) as $\delta\mathrm{AC} = \mathrm{AC}^t - \mathrm{AC}^h$ and $\delta\phi = \phi^t - \phi^h$, respectively.

All measured signals contain some form of noise. In optical tomographic imaging systems, certain types of noise, such as that originating from inaccurate positioning of detectors and sources, can be eliminated by careful calibration. Other noise forms, such as Johnson noise or shot noise, which are intrinsic phenomena in all electronic circuits, are impossible to avoid. Theoretical and experimental analyses of these noise models and how they affect optical measurement systems have been given by Toronov *et al.*[18] and by Tao *et al.*[25] When one considers small imaging domains, the optical signals are usually relatively strong, and thus shot noise is the dominant noise source. This allows us, in this study, to rely on the analysis provided by Toronov *et al.*[18] who derived the following expressions for the noises (standard deviations of sig-

nal fluctuation) in the DC intensity (σ_{DC}), AC amplitudes (σ_{AC}), and phase (σ_ϕ) measurements:

$$\sigma_{DC} \propto \sqrt{\langle DC \rangle}, \tag{16}$$

$$\sigma_{AC} \propto \sqrt{\langle DC \rangle}, \tag{17}$$

$$\sigma_\phi \propto \frac{1}{\langle AC \rangle / \sigma_{AC}} \propto \frac{\langle AC \rangle}{\sqrt{\langle DC \rangle}}, \tag{18}$$

where DC, AC, and ϕ are the DC intensity, the AC amplitude, and the phase measurements, respectively, in the experiment. The $\langle\ \rangle$ denote an ensemble measurement average.

C. Signal-to-Noise Ratio and Signal-Sensitivity-to-Noise Ratio

With the above signal and noise models in place, we can define the term SNR for the AC amplitude and phase as follows:

$$\mathrm{SNR}_{AC}(\omega) = \frac{\langle AC \rangle}{\sigma_{AC}} \propto \frac{\langle AC \rangle}{\sqrt{\langle DC \rangle}}, \tag{19}$$

$$\mathrm{SNR}_\phi(\omega) = \frac{\langle \phi \rangle}{\sigma_\phi} \propto \frac{\langle \phi \rangle}{\sigma_{AC}/\langle AC \rangle} \propto \langle \phi \rangle \mathrm{SNR}_{AC}. \tag{20}$$

Therefore the SNR is the ratio of the signal divided by the noise in the measurements, given by the standard deviation σ. The value of the SNR is important if we want to determine the quality of a signal available for a given tissue geometry and composition. If we want to determine whether a heterogeneity is detectable, we need to look at the effect this heterogeneity has on the measurements. Therefore we define SSNR for the AC amplitude (SSNR_{AC}) and phase (SSNR_ϕ) as follows:

$$\mathrm{SSNR}_{AC}(\omega) = \frac{\langle \delta AC \rangle}{\sigma_{AC}} \propto \frac{\langle AC^t \rangle - \langle AC^h \rangle}{\sqrt{\langle DC \rangle}}, \tag{21}$$

$$\mathrm{SSNR}_\phi(\omega) = \frac{\langle \delta\phi \rangle}{\sigma_\phi} \propto (\langle \phi^t \rangle - \langle \phi^h \rangle) \mathrm{SNR}_{AC}. \tag{22}$$

Here the SSNR is the ratio of the signal sensitivity (AC sensitivity δAC, or phase sensitivity $\delta\phi$) divided by the noise in the measurement. Note that both SNR and SSNR are frequency dependent, as AC amplitude and phase are frequency dependent.

3. Numerical Frequency Sensitivity Analysis

Figure 1 illustrates a general tissue geometry used throughout this work. The computational domain is defined by $\mathcal{D} := \{(x, y, z)^T | x^2 + y^2 \le 1; 0 \le z \le 2\}$. In the simulations we place a point source at $\mathbf{x}_s = (1, 0, 1)^T$. Detectors are evenly distributed on a circle defined by $\Gamma := \{(x, y, z)^T | x^2 + y^2 = 1; z = 1\}$. We refer to specific detectors by numbering them counterclockwise from 1 through 12 starting at source position S. The domain is discretized into approximately 17,000 tetrahedral elements and 48 directions (S6, with full level symmetry). A cylindrical heterogeneity with varying diameter and optical properties is placed at various distances off center.

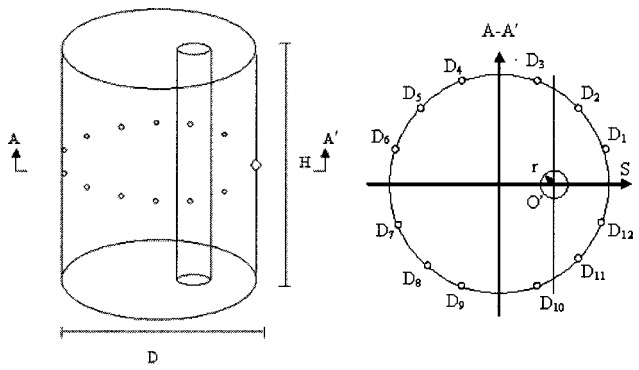

Fig. 1. Geometric setup for numerical simulation, the diameter of the cylinder $D = 2$ cm, and height $H = 2$ cm. The source is identified by the letter S and the detectors by circles.

A. Homogeneous Media

Before investigating the influence of optical inhomogeneities on frequency-domain data, we studied the effect of source-modulation frequencies on the boundary measurement of a homogeneous domain. Therefore in this case the cylindrical inhomogeneity in Fig. 1 has the same optical properties ($\mu_a = 0.05\ \mathrm{cm}^{-1}$, $\mu_s = 10.0\ \mathrm{cm}^{-1}$, and $g = 0.7$) as the surrounding medium. Using our transport-theory-based code, we calculated the amplitude and phase delays observed on the 12 detector positions. Figures 2(a) and 2(b) show the amplitude values and phase delays for different modulation frequencies at detector positions 1 to 6 (see also Fig. 1). As expected, it can be seen that

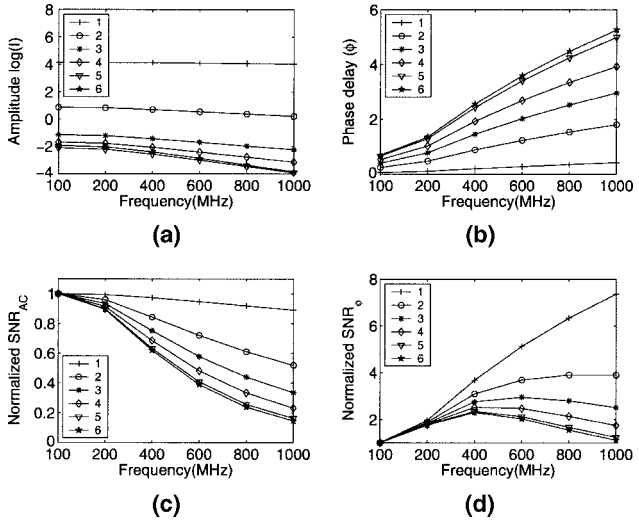

Fig. 2. (a) Amplitude and (b) phase delay as well as (c) SNR_{AC} and (d) SNR_ϕ of a homogeneous cylinder at modulation frequencies from 100 to 1000 MHz. Here 1 to 6 refer to the detectors arranged around the boundary, 1 being the closest detector to the source and 6 the farthest from the source (see also Fig. 1).

Table 1. Summary of Different Cases Used for Sensitivity Analysis with Absorption Perturbations

	Test Cases[a]	μ_a (cm^{-1})	μ_s (cm^{-1})	r (cm)	OO' (cm)
Reference	$2.0\mu_a{}^b$, $r = 0.25$ cm, $OO' = 0.50$ cm	0.1	10.0	0.25	0.5
Strength	$1.2\mu_a{}^b$	0.06	10.0	0.25	0.5
	$1.5\mu_a{}^b$	0.075	10.0	0.25	0.5
Size	$r = 0.15$ cm	0.1	10.0	0.15	0.5
	$r = 0.35$ cm	0.1	10.0	0.35	0.5
Location	$OO' = 0.0$ cm	0.1	10.0	0.25	0.0
	$OO' = 0.25$ cm	0.1	10.0	0.25	0.25

[a]Here μ_a and μ_s are absorption and scattering coefficients, and OO' is the offset of the perturbation center from the homogeneous background center. For all the cases, the background optical properties are set with $\mu_a{}^b = 0.05\ cm^{-1}$, $\mu_s{}^b = 10.0\ cm^{-1}$, and $g = 0.7$.

as the modulation frequency increases, the amplitude decreases while the phase delay increases. Furthermore when the detector is farther away from the source, the amplitude on the detector is smaller, and the phase is larger. These behaviors are not surprising as they are readily observed in many phenomena involving wave propagation.

The amplitude and phase SNRs on different detectors are plotted in Figs. 2(c) and 2(d). Since the noise model given in the previous subsection is a proportional formula, no absolute values of the SNR or SSNR can be obtained. Hence here and in the following sections, the SNR and SSNR curves are all normalized to the respective values at 100 MHz. Note that with an increase of the modulation frequency, the SNR_{AC}s are decreasing at all detector positions. The reason behind this is the decreasing AC amplitude and the constant noise with respect to the modulation frequency [see Eq. (17)]. The phase SNR_ϕs reach the maximal values between 400 and 600 MHz, except for detectors 1 and 2, which are the closest to the source.

After having presented some basic results for homogeneous media, we now investigate heterogeneous media. As can be seen in Eq. (10), the signal sensitivity (δJ) depends on the changes in absorption ($\delta\mu_a$) and scattering perturbation ($\delta\mu_s$) and both contribute to the signal sensitivity independently. Therefore we will present the effects of absorption and scattering heterogeneities in separate subsections.

B. Signal-Sensitivity-to-Noise Ratio Studies with Absorbing Perturbations

We start by examining the effects of absorption perturbations. In these cases, only the absorption property of the heterogeneity is varied. The scattering property of the heterogeneity is identical to that of the background medium. The signal's amplitude sensitivity $\langle\delta AC\rangle$ and phase sensitivity $\langle\delta\phi\rangle$ are determined as functions of different absorption coefficients, sizes, and locations of the heterogeneity. We vary the source-modulation frequency and show the SSNR curves for the different detector locations. A summary of all cases studied is listed in Table 1.

In Figs. 3(a) and 3(b), δAC and $\delta\phi$ at different detector positions as functions of the modulation frequencies are plotted for the reference case (see Table 1). Here δAC decreases as the modulation frequency increases or as the distance between a detector and source pair increases. $|\delta\phi|$ shows increases as the modulation frequency increases.

Figures 3(c) and 3(d) show the normalized SSNRs for the reference case at different detector positions as functions of the modulation frequency. Again, all these SSNR curves are normalized to the 100 MHz point. Increasing the modulation frequency leads to a decrease in the $SSNR_{AC}$ [see Fig. 3(c)]. This is in accordance with Eq. (21) because the signal's amplitude sensitivity (δAC) decreases with the modulation frequency, and at the same time the AC amplitude noise (δ_{AC}) is constant. Rather than showing a steady decrease, the $SSNR_\phi$s reach distinct maxima at 400 MHz for all detector positions. That a maximum occurs in the $SSNR_\phi$ can be understood by looking at Eq. (22). The $SSNR_\phi$ is proportional to the ratio of the signal's phase sensitivity ($\delta\phi$) and the phase noise (σ_ϕ). As the modulation frequency increases, both $\delta\phi$ and (σ_ϕ) increase, leading to some characteristic maxima in these $SSNR_\phi$ curves.

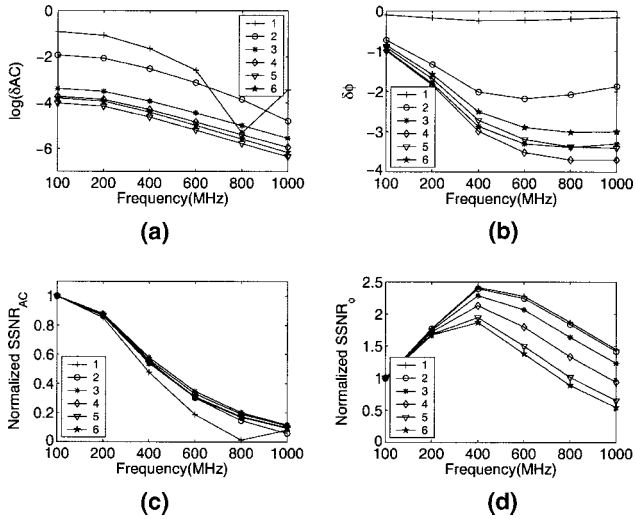

Fig. 3. (a) Signal amplitude sensitivity (δAC), (b) phase sensitivity ($\delta\phi$), (c) $SSNR_{AC}$, and (d) $SSNR_\phi$ of the reference case listed in Table 1. Here 1 to 6 refer to the detectors arranged around the boundary, 1 being the closest detector to the source and 6 the farthest from the source (see also Fig. 1).

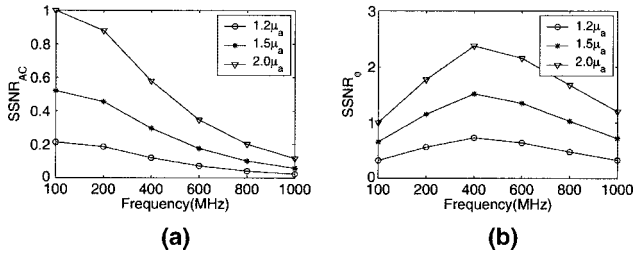

Fig. 4. (a) $SSNR_{AC}$ and (b) $SSNR_{\phi}$ with varied strengths of absorption perturbation, $1.2\mu_a$, $1.5\mu_a$, $2.0\mu_a$.

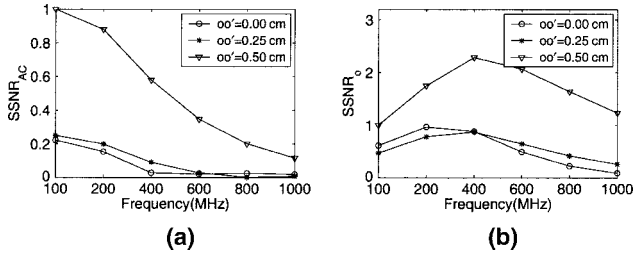

Fig. 6. (a) $SSNR_{AC}$ and (b) $SSNR_{\phi}$ by moving the location of absorption perturbation $OO' = 0.0$, 0.25, and 0.50 cm.

1. Absorption Perturbation Strength

To investigate how changes in the absorption perturbation affect the SSNRs, we select the readings of just one representative detector (in this case detector 3) to limit the amount of data shown in one graph. In the reference case (described in Subsection 3.B) the absorption coefficient of the perturbation is two times higher than that of the background medium. Now we add cases in which the absorption coefficients inside the heterogeneity are 1.5 and 1.2 times higher than that in the background medium. Figures 4(a) and 4(b) graph the $SSNR_{AC}$ and $SSNR_{\phi}$, respectively. We observe that in the $SSNR_{AC}$ and $SSNR_{\phi}$ plots, as the absorption inside the heterogeneity is increased, the SSNR values increase. However, while the $SSNR_{AC}$ decreases monotonically as the source modulation is increased, the $SSNR_{\phi}$ plots show distinct maxima at 400 MHz.

2. Absorption Perturbation Size

Next, we examine how changes in the size of a heterogeneity influence the SSNRs on the detectors. Cylindrical perturbations with radii of 0.15 cm, 0.25 cm (reference case), and 0.35 cm were tested. The results for these cases are shown in Figs. 5(a) and 5(b). As expected, we observed that with increasing perturbation size the $SSNR_{AC}$ and $SSNR_{\phi}$ increase. Again, the $SSNR_{AC}$ monotonically decreases with modulation frequency with all perturbation sizes, while the $SSNR_{\phi}$ curves show maxima at ~400 MHz.

3. Absorption Perturbation Location

Here we examine how perturbation location affects the system's detection limitation. The center of the perturbation (O') was placed in different locations ($OO' = 0.0$ cm, 0.25 cm (reference case), and 0.5 cm) on line OS in Fig. 1. The perturbation strength ($2.0\mu_a$) and size ($r = 2.5$ mm) were fixed, while the source modulation frequencies varied from 100 to 1000 MHz. The results are shown in Figs. 6(a) and 6(b). The $SSNR_{AC}$s monotonically decrease with the modulation frequency at different OO', and the $SSNR_{\phi}$s show maxima at 200–400 MHz depending on the position of the perturbation center. These two graphs also reveal that the SSNR values become increasingly larger when the heterogeneity gets closer to the source. Therefore it is easier to detect the presence of the heterogeneity when it is closer to the source.

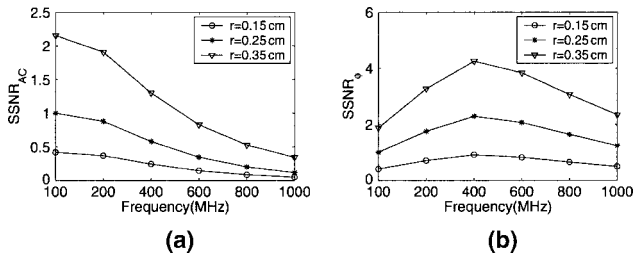

Fig. 5. (a) $SSNR_{AC}$ and (b) $SSNR_{\phi}$ with varied sizes of absorption perturbation, $r = 0.15$, 0.25, and 0.35 cm.

C. Signal-Sensitivity-to-Noise Ratio Studies with Scattering Perturbations

Physically, light absorption is a phenomenon in which photons are eliminated, while light scattering is a phenomenon in which the trajectories of the photons are changed. Thus changing a tissue's absorption properties decreases (or increases) the amount of photons arriving at the detectors, while changing a tissue's scattering properties will redistribute the number of photons that arrive at the different detectors.

Here we examine cases where the scattering property of the heterogeneity varies, while the absorption property of the heterogeneity is constant and identical to that of the background medium. A summary of all cases used in the numerical experiments can be found in Table 2.

As in the study of the absorption perturbation, the reference case was analyzed first. Investigating the δAC and $\delta\phi$ with scattering perturbation shown in Figs. 7(a) and 7(b), we find the signal's sensitivity trends to differ from those caused by absorption perturbation. The δACs are almost independent of the modulation frequency at the detectors close to the source [Fig. 7(a), detectors 1 and 2]. For the detectors farther away from the source, more complex frequency dependences are observed, as some detectors (3 and 4) monotonically increase, while others take on minimal values between 200–400 MHz (detectors 5 and 6). In general, the $\delta\phi$'s increase with the modulation frequency, except for detector 2.

Figures 7(c) and 7(d) show the $SSNR_{AC}$ and $SSNR_{\phi}$, respectively. In most cases the $SSNR_{AC}$ curves show maxima for source-modulation frequencies between 400 and 600 MHz. However, the $SSNR_{AC}$ curves for detectors 5 and 6, both far away from the source, have

Table 2. Summary of Different Cases Used for Sensitivity Analysis with Scattering Perturbations

	Test Cases[a]	μ_a (cm^{-1})	μ_s (cm^{-1})	r (cm)	OO' (cm)
Reference	$2.0\mu_s{}^b$, $r = 0.25$ cm, $OO' = 0.50$ cm	0.05	20.0	0.25	0.5
Strength	$1.2\mu_s{}^b$	0.05	12.0	0.25	0.5
	$1.5\mu_s{}^b$	0.05	15.0	0.25	0.5
Size	$r = 0.15$ cm	0.05	20.0	0.15	0.5
	$r = 0.35$ cm	0.05	20.0	0.35	0.5
Location	$OO' = 0.0$ cm	0.05	20.0	0.25	0.0
	$OO' = 0.25$ cm	0.05	20.0	0.25	0.25

[a]Here μ_a and μ_s are absorption and scattering coefficients, and OO' is the offset of the perturbation center from the homogeneous background center. For all the cases, the background optical properties are set with $\mu_a{}^b = 0.05\ cm^{-1}$, $\mu_s{}^b = 10.0\ cm^{-1}$, and $g = 0.7$.

some minimal values at 200 and 400 MHz, respectively. The $SSNR_\phi$ curves all show maximal values at 400 MHz, except the curve for detector 1, which strongly increases after it takes on a minimum value at 200 MHz.

1. Scattering Perturbation Strength

In Figs. 8(a) and 8(b), $SSNR_{AC}$s and $SSNR_\phi$s are plotted for the case when the scattering coefficients in the heterogeneity vary from 12.0 to 20.0 cm^{-1} corresponding to the contrast ratio between 1.2 and 2.0. Similar to the case of the absorption perturbation, we observe that the SSNRs increase with the strength of the perturbation. However, the $SSNR_{AC}$s with scattering perturbations show maximal values at approximately 600 MHz, while in the absorption perturbation cases the $SSNR_{AC}$s monotonically decreased with the increasing modulation frequency. The $SSNR_\phi$ curves again reach maximal values at 400 MHz.

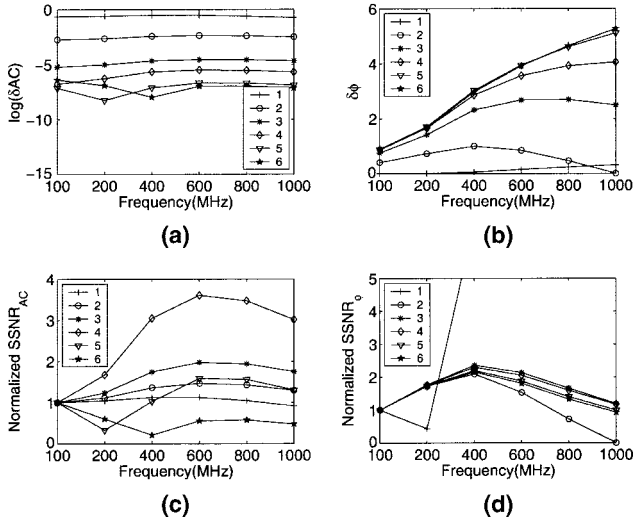

Fig. 7. (a) Signal amplitude sensitivity (δAC) and (b) phase sensitivity (δϕ) and as well as (c) $SSNR_{AC}$, and (d) $SSNR_\phi$ of the reference case listed in Table 2. Here 1 to 6 refer to the detectors arranged around the boundary, 1 being the closest detector to the source and 6 the farthest from the source (see also Fig. 1).

2. Scattering Perturbation Size

The impacts of the size of the scattering perturbations are plotted in Figs. 9(a) and 9(b). From these plots, we find that $SSNR_\phi$s improve with the enlargement of the perturbation size. Compared with previous cases, all $SSNR_\phi$s keep their peak values at 400 MHz, while the position of the maximum in the $SSNR_{AC}$ curves moves from 600 to 800 MHz.

3. Scattering Perturbation Location

Changing the position of the perturbation leads to a shift of the maximum in the $SSNR_{AC}$ and $SSNR_\phi$ curves (see Fig. 10). As mentioned before, scattering is a phenomenon of redistributing photons, thus, the location of the perturbation affects the different detector signal sensitivities. In Fig. 10(a), the centrally located perturbation reaches its maximum $SSNR_{AC}$ at the low modulation frequency, while in the cases of off-center perturbation, the maximal $SSNR_{AC}$ values are reached at a higher frequency. The $SSNR_\phi$ is more complicated. Figure 10(b) shows that deep embedded perturbation ($OO' = 0.0$ cm) has a much lower SSNR compared with that near the surface

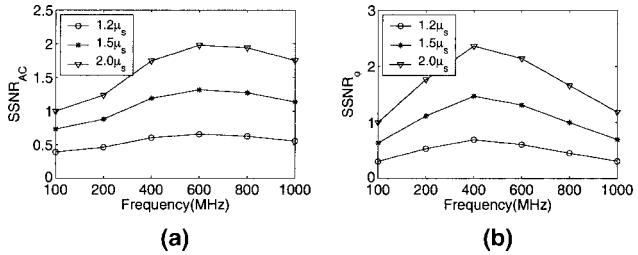

Fig. 8. (a) $SSNR_{AC}$ and (b) $SSNR_\phi$ with varied strengths of scattering perturbation, $1.2\mu_s$, $1.5\mu_s$, $2.0\mu_s$.

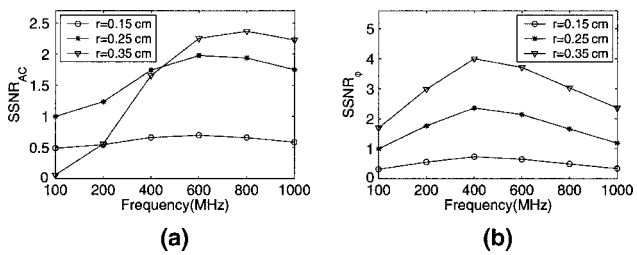

Fig. 9. (a) $SSNR_{AC}$ and (b) $SSNR_\phi$ with varied sizes of scattering perturbation, $r = 0.15$, 0.25, and 0.35 cm.

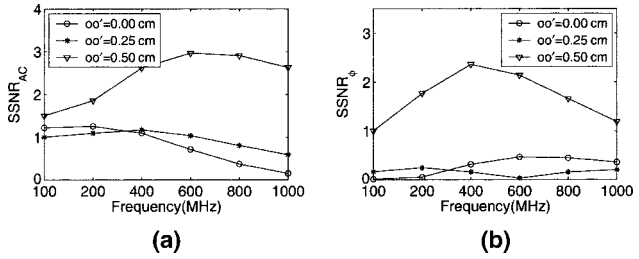

Fig. 10. (a) $SSNR_{AC}$ and (b) $SSNR_{\phi}$ by moving the location of scattering perturbation, $OO' = 0.0$, 0.25, and 0.50 cm.

($OO' = 0.5$ cm), which means it is hard to detect and characterize the centrally located perturbations.

4. Discussion and Conclusions

We focused on the sensitivity analysis concerning the effects of optical heterogeneities in a cylindrical volume, which mimics small geometries frequently encountered in optical tomographic imaging of small animals or human fingers. The analysis was based on solutions to the frequency-domain equation of radiative transfer, which provides more accurate results than the widely employed diffusion approximation. Using different source modulation frequencies, we studied the effects of size, location, strength, and optical properties on the detectability of embedded heterogeneities.

Analyzing the signal-sensitivity-to-noise ratios (SSNRs) for various cases, we found that we could distinguish four different situations: two for the case of an absorbing heterogeneity and two for the case of a scattering heterogeneity. If the heterogeneity is purely absorbing, the $SSNR_{AC}$ is always largest for a modulation frequency of 0 Hz. This result is not surprising and is in agreement with previous work by other groups.[17,18] However, the $SSNR_{\phi}$ consistently shows an optimal value for source-modulation frequencies at ~400 MHz. While the phase delay is monotonically increasing with increasing modulation frequency, this does not automatically lead to more and more accurate phase measurements; the noise (defined as standard deviation) in the phase measurements is also increasing with increasing modulation frequency. Combining these two effects results in an optimal modulation frequency for which the $SSNR_{\phi}$ is largest.

When scattering heterogeneities are considered a more complex picture occurs. Now even the $SSNR_{AC}$ shows optimal values at nonzero modulation frequencies. While the $SSNR_{\phi}$ is again the largest for modulation frequencies at approximately 400 MHz, for most situations considered in this study, the best $SSNR_{AC}$ is obtained for a variety of values between 200 and 800 MHz, depending on the size and location of the heterogeneity inside the medium. These findings suggest that a frequency-domain optical tomographic imaging system for small animal and finger joint studies should focus on source-modulation frequencies below 800 MHz. If only one frequency is to be used, 400 MHz appears optimal. However, a multifrequency system that allows us to perform amplitude measurements at various frequencies ranging from 0 to 800 MHz, and phase measurements between 300 and 500 MHz promises to capture most types of effects.

We thank James Masciotti and Hilary Libka for many useful discussions and helpful suggestions concerning this manuscript. This work was supported in part by grants from the National Institute of Arthritis and Musculoskeletal and Skin Diseases (NIAMS-2R01-AR046255) and the National Institute of Biomedical Imaging and Bioengineering (NIBIB-R01EB001900), which are both divisions of the National Institutes of Health (NIH).

References

1. B. Chance, R. R. Alfano, B. J. Tromberg, M. Tamura, and E. M. Sevick-Muraca, in *Optical Tomography and Spectroscopy of Tissue VI,* Proc. SPIE **5693** (2005).
2. B. Chance, R. R. Alfano, and B. J. Tromberg, in *Optical Tomography and Spectroscopy of Tissue III,* Proc. SPIE **3597,** (1999).
3. G. Müller, B. Chance, R. R. Alfano, S. Arridge, J. Beuthan, E. Gratton, M. Kaschke, B. Masters, S. Svanberg, and P. van der Zee, in *Medical Optical Tomography: Functional Imaging and Monitoring,* Proc. SPIE **IS11** (1993).
4. A. K. Scheel, M. Backhaus, A. D. Klose, B. Moa-Anderson, U. Netz, K. G. Hermann, J. Beuthan, G. A. Müller, G. R. Burmester, and A. H. Hielscher, "First clinical evaluation of sagittal laser optical tomography for detection of synovitis in arthritic finger joints," Ann. Rheum. Dis. **64,** 239–245 (2005).
5. A. H. Hielscher, A. Klose, A. K. Scheel, B. Moa-Anderson, M. Backhaus, U. Netz, and J. Beuthan, "Sagittal laser optical tomography for imaging of rheumatoid finger joints," Phys. Med. Biol. **49,** 1147–1163 (2004).
6. A. H. Hielscher, "Optical tomographic imaging of small animals," Curr. Opin. Biotechnol. **16,** 79–88 (2005).
7. O. Dorn, "A transport–backtransport method for optical tomography," Inverse Probl. **14,** 1107–1130 (1998).
8. A. D. Klose and A. H. Hielscher, "Iterative reconstruction scheme for optical tomography based on the equation of radiative transfer," Med. Phys. **26,** 1698–1707 (1999).
9. A. D. Klose, U. Netz, J. Beuthan, and A. H. Hielscher, "Optical tomography using the time-independent equation of radiative transfer. part 1: Forward model," J. Quant. Spectrosc. Radiat. Transfer **72,** 691–713 (2002).
10. A. D. Klose and A. H. Hielscher, "Optical tomography using the time-independent equation of radiative transfer. part 2: Inverse model," J. Quant. Spectrosc. Radiat. Transfer **72,** 715–732 (2002).
11. A. D. Klose and A. H. Hielscher, "Quasi-Newton methods in optical tomographic image reconstruction," Inverse Probl. **19,** 387–409 (2003).
12. G. Abdoulaev and A. H. Hielscher, "Three-dimensional optical tomography with the equation of radiative transfer," J. Electron. Imaging **14,** 594–560 (2003).
13. K. Ren, G. S. Abdoulaev, G. Bal, and A. H. Hielscher, "Algorithm for solving the equation of radiative transfer in the frequency domain," Opt. Lett. **29,** 578–580 (2004).
14. K. Ren, G. Bal, and A. H. Hielscher, "Frequency domain optical tomography with the equation of radiative transfer," SIAM J. Sci. Comput. (USA) **28,** 1463–1489 (2006).
15. S. R. Arridge and W. R. B. Lionheart, "Nonuniqueness in diffusion-based optical tomography," Opt. Lett. **23,** 882–884 (1998).
16. T. O. McBride, B. W. Pogue, U. L. Österberg, and K. D.

Paulsen, "Separation of absorption and scattering heterogeneities in NIR tomographic imaging of tissue," in *Biomedical Topical Meetings,* 2000 OSA Technical Digest Series (Optical Society of America, 2000), pp. 339–341.
17. D. A. Boas, M. A. O'Leary, B. Chance, and A. G. Yodh, "Detection and characteriztion of optical inhomogeneities with diffuse photon density waves: a singal-to-noise analysis," Appl. Opt. **36,** 75–92 (1997).
18. V. Toronov, E. D'Amico, D. Hueber, E. Gratton, B. Barbieri, and A. Webb, "Optimization of the signal-to-noise ratio of frequency-domain instrument for near-infrared spectro-imaging of the human brain," Opt. Express **11,** 2117–2729 (2003).
19. M. J. Eppstein F. Fedele, and J. P. Laible, "Coupled complex adjoint sensitivities for frequency-domain fluorescence tomography: Theory and vectorized imlementation," J. Comput. Phys. **187,** 597–619 (2003).
20. L. G. Henyey and J. L. Greenstein, "Diffuse radiation in the galaxy," Astrophys. J. **90,** 70–83 (1941).
21. A. J. Welch and M. J. C. Van Gemert, *Optical-Thermal Response of Laser-Irradiated Tissue* (Plenum, 1995), Chap. 6.
22. E. E. Lewis and W. F. Miller, *Computational Methods of Neutron Transport,* 2nd ed. (American Nuclear Society, 1993).
23. R. Eymard, T. Gallouet, and R. Herbin, "Finite volume methods," in *Handbook of Numerical Analysis VII,* P. Ciarlet and J. L. Lions, eds., 2nd ed. (North-Holland, 2000).
24. Y. Saad and M. H. Schultz, "GMRES: A generalized minimal residual algorithm for solving nonsymmetric linear systems," SIAM (Soc. Ind. Appl. Math) J. Sci. Stat. Comput. **7,** 856–869 (1986).
25. T. Tao, Y. Chen, J. Zhang, X. Intes, and B. Chance, "Analysis on performance and optimization of frequency-domain near-infrared instruments," J. BioMed. Opt. **7,** 643–649 (2002).